

A deeper view of Extremely Red Galaxies: the redshift distribution in the GOODS/CDFS ISAAC field.

K.I. Caputi ^{*}, J.S. Dunlop [†], R.J. McLure [‡] and N.D. Roche [§]

Institute for Astronomy, University of Edinburgh, Royal Observatory, Edinburgh EH9 3HJ, Scotland, U.K.

arXiv:astro-ph/0401047v1 6 Jan 2004

ABSTRACT

We have analysed 5-epoch GOODS HST-ACS B, V, I₇₇₅ and z datasets (V1.0 release), in conjunction with existing VLT-ISAAC imaging in the J, H and K_s bands, to derive estimated redshifts for the sample of 198 Extremely Red Galaxies (ERGs) with K_s < 22 (Vega) and (I₇₇₅ – K_s) > 3.92 selected by Roche et al. (2003) from 50.4 arcmin² of the GOODS/CDFS field. We find that, at this depth, the ERG population spans the redshift range 0.5 < z_{phot} < 5.0 and over two decades in mass ($\sim 3 \times 10^9 M_{\odot}$ to $\sim 3 \times 10^{11} M_{\odot}$). Our results show that the dust-corrected red envelope of galaxy evolution is well modelled by a starburst at redshift z_f = 5 followed thereafter by a passive evolution. We explore the evolution of the ERG luminosity function (LF) from redshifts $\langle z_{\text{phot}} \rangle = 1.0$ to $\langle z_{\text{phot}} \rangle = 2.5$ and compare it with the global K_s-band LF at redshifts $1 < z_{\text{phot}} < 2$. We find that the bright end of the ERG LF does not decrease from redshifts $\langle z_{\text{phot}} \rangle = 2.0$ to $\langle z_{\text{phot}} \rangle = 2.5$ and we connect this fact with the presence of progenitors of the local L > L* population at redshifts z_{phot} > 2. We have investigated the existence of high-redshift Lyman break galaxies massive enough to be included in this ERG sample. Out of an initial list of 12 potential very high redshift candidates, we have identified 5 ERGs which have a very high probability of lying at z_{phot} > 4. 4/5 of these objects are very massive ($> 10^{11} M_{\odot}$) and could account for a comoving density of progenitors of local L > L* galaxies of $\rho_c \approx (2.9 \pm 1.5) \times 10^{-5} \text{ Mpc}^{-3}$. Finally, we discuss the advantages of multi-colour to single-colour selection techniques in obtaining reliable lists of very high-redshift candidate sources, and present revised lower redshift estimates for four sources previously claimed as potential z > 5 dropouts in recent studies.

Key words: galaxies: evolution – galaxies: formation – galaxies: high-redshift

1 INTRODUCTION

The study of ‘extremely red galaxies’ (ERGs) is of importance for setting constraints on the first epoch of massive galaxy formation, for exploring the population of dust-reddened starbursts, and for testing models of galaxy formation in general. Usually defined as objects with R – K > 5 or I – K > 4 (Vega), these galaxies have been widely studied since their discovery by Elston, Rieke & Rieke (1988). The traditional picture identifies the ERGs either with passively evolving elliptical galaxies, or with young starbursts strongly reddened by dust. This mixture has been confirmed by spectroscopic (Dunlop et al. 1996; Soifer et al. 1999; Cimatti et al. 2002; Saracco et al. 2003a) and sub-millimetre surveys

(Cimatti et al. 1998; Dey et al. 1999; Wehner, Barger & Kneib 2002). However, the latest photometric and morphological studies of these objects indicate that the ERG population is perhaps more complex than previously considered (Smail et al. 2002; Miyazaki et al. 2002; Yan & Thompson 2003; Moustakas et al. 2003).

Most previous samples of ERGs have been selected to a limiting magnitude of K_s = 20 or brighter, and their inferred redshift distributions peak at z ∼ 1 – 2. New deeper observations reaching K_s = 22 and beyond (Maihara et al. 2001, Saracco et al. 2001) are uncovering ERGs at higher redshifts. In particular, a population of galaxies with very red near-infrared colours J – K_s > 3 has been discovered to lie at redshifts z > 2 (Totani et al. 2001). Saracco et al. (2003b) claim that three massive galaxies of this kind in the Hubble Deep Field South (HDFS) at $\langle z_{\text{phot}} \rangle = 2.7$ account for at least 40% of the comoving density of the local L > L* galaxies. However, these studies are based on small area surveys which cover a few square arcmin of the sky. Deep K_s-band

^{*} kic@roe.ac.uk

[†] jsd@roe.ac.uk

[‡] rjm@roe.ac.uk

[§] ndr@roe.ac.uk

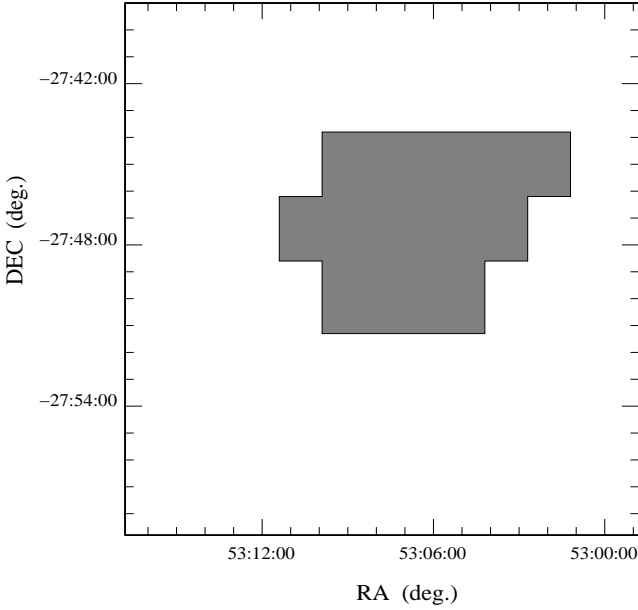


Figure 1. Schematic diagram of the sub-region covered by deep VLT/ISAAC near-infrared imaging (shaded area) within the larger GOODS/CDFS field with full HST-ACS coverage.

observations in wider areas are required to obtain significant samples of high redshift ERGs and to determine more accurate lower limits for the fraction of massive galaxies already assembled at different redshifts. Some of these ‘hyper extremely’ red galaxies have been found to be counterparts of sub-millimetre-selected galaxies (Frayer et al. 2003), which are known to be mainly located at redshifts $2 < z < 4$ (Dunlop 2001, Aretxaga et al. 2003, Chapman et al. 2003).

The Great Observatories Origins Deep Survey (GOODS) (Dickinson et al. 2003a) is providing unprecedented multiwavelength data in ~ 320 arcmin 2 centred on the Chandra Deep Field South (CDFS) and Hubble Deep Field North (HDFN). Within the GOODS/CDFS field, Roche, Dunlop & Almaini (2003) selected 198 ERGs with $K_s < 22$ (Vega) and $I_{775} - K_s > 3.92$ from the 50.4 arcmin 2 for which deep near infra-red (near-IR) data have been obtained with the Infrared Spectrometer and Array Camera (ISAAC) on the ‘Antu’ Very Large Telescope (Antu-VLT). This is the deepest significant sample of ERGs selected to date, and is the subject of the present study. The region covered by the ISAAC observations within the GOODS/CDFS field is shown in fig.1. Other previous studies of ERGs reaching $K_s \sim 20$ exist in the CDFS. For example, the K20 survey has yielded spectroscopic redshifts for ERGs in 32.2 arcmin 2 of this field (Cimatti et al. 2002). More recently, the GOODS team (Moustakas et al. 2003) selected a sample of ERGs from 163 arcmin 2 of the GOODS/CDFS field with data from the Advanced Camera for Surveys (ACS) on board the Hubble Space Telescope (HST). The area covered by this brighter ERG sample is three times greater than that covered by the Roche et al. sample studied here. However, the Moustakas et al. sample only reaches a depth of $K_s \sim 20.2$ (equivalent to $K_s = 22$, AB), and so the present study probes a different (and complementary) region of parameter space to that already explored by the GOODS team.

Roche et al. (2003) studied the number density of ERGs within their $K_s = 22$ sample and compared the results with the predictions of different galaxy formation models. They also demonstrated that the strong clustering displayed by the ERG population extends to the faintest K_s magnitudes. In this work, we present photometric redshift estimates for the ERGs in the Roche et al. sample and explore the resulting implications for the nature and evolution of ERGs.

The layout of this paper is as follows. First, in Section 2, we briefly review the sample selection and explain the details of the multiwavelength photometry. In Section 3 we discuss the photometric redshift techniques applied, and present examples of individual redshift determinations. Then, in Section 4 we present our results and discuss raw and dust-corrected Hubble diagrams ($K_s - z_{\text{phot}}$), the red envelope of galaxy evolution, the evolution of the ERG luminosity function (LF), and derived lower limits on the comoving densities of progenitors of local $L > L^*$ galaxies. We also discuss the individual properties of each of our high-redshift ($z > 4$) candidate sources, and review the existence of an ERG cluster reported by Roche et al. (2003). Finally, we present some concluding remarks in Section 5. We adopt throughout a cosmology with $H_0 = 70 \text{ km s}^{-1} \text{Mpc}^{-1}$, $\Omega_M = 0.3$ and $\Omega_\Lambda = 0.7$.

2 THE SAMPLE-MULTIWAVELENGTH PHOTOMETRY

GOODS observations include optical and near-IR imaging in the B, V, I_{775} and z bands with the ACS/HST and J, H and K_s bands with the ISAAC-VLT. Roche et al. (2003) used ISAAC K_s -band data and ACS I_{775} -band data to select a sample of 198 ERGs with $K_s < 22$ (Vega) and $I_{775} - K_s > 3.92$. They performed the source extraction in the K_s band and photometry in the I_{775} , J, H and K_s bands using the public code ‘SExtractor’ (Bertin & Arnouts, 1996). All the selected ERGs are at least 3σ detections on the K_s -band images. Further details of their photometric measurements from the ground-based data and their preliminary measurements on the I_{775} -band ACS images are given in their paper. The aperture magnitudes measured on ISAAC images by Roche et al. (2003) and used here correspond to 2''-diameter in all cases.

We performed photometric measurements for the four ACS bands on the stacked GOODS 5-epoch images (V1.0 HST/ACS data release), using the corresponding weighting maps. We looked for counterparts of the K_s -selected ERGs on the I_{775} and z -band images within an angular radius of 1''. For B and V bands we restricted the search of counterparts to 0.5'' to minimise the presence of interlopers. We also performed the magnitude measurements using the public code ‘SExtractor’. Many ERGs appeared as non-detected in the B and V bands, and some of them as non-detected in the I_{775} or z bands. The algorithms for computing photometric redshifts depend critically on the adopted value of limiting magnitudes in the case of non detections, and a careful treatment of potential ‘dropouts’ is necessary to prevent the photometric redshift algorithms from finding fake high redshift sources. Therefore, in each case of a ‘SExtractor’ non-detection, we used the IRAF task ‘phot’ to measure aperture magnitudes centred at the ERG K_s -band po-

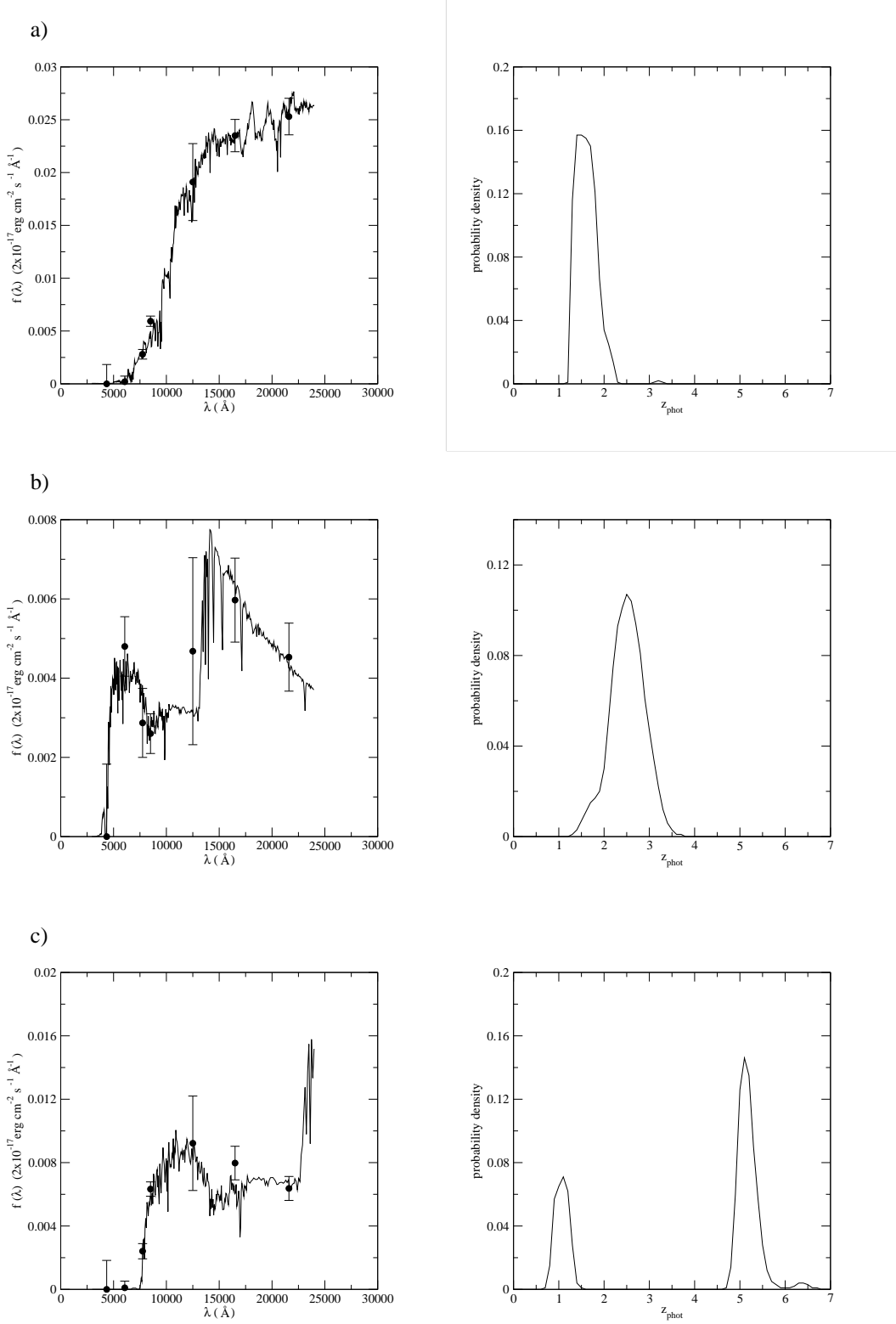


Figure 2. Example spectral energy distributions (left-hand plots) and redshift probability density distributions (right-hand plots) for three ERGs in the Roche et al. sample. a) an ERG with ‘hyperz’ primary solution $z_{\text{phot}} = 1.40$, b) an ERG with primary solution $z_{\text{phot}} = 2.52$, c) an ERG with primary solution $z_{\text{phot}} = 5.07$. The circles in the SED plots correspond to the measured aperture magnitudes in each filter. The solid-line curves indicate the best-fit template in each case.

sition. We measured 2''-diameter aperture magnitudes on each ACS filter for those ERGs with $z_{2''} < 26$ (AB). Beyond $z_{2''} = 26$ (AB), we found that little flux was missed using 1'' instead of 2''-diameter aperture magnitudes. Thus, for objects with $z_{2''} > 26$ (AB), we used 1''-diameter aperture magnitudes to reduce the random errors, and corrected the values systematically using the average offset between the 2'' and 1''-diameter aperture magnitudes measured in each $\Delta = 1$ magnitude bin. After this procedure, only a few objects remained as formally non-detected in the V or redder ACS bands.

3 REDSHIFT ESTIMATIONS

We computed photometric redshifts for the ERGs in the Roche et al. (2003) sample with the public code ‘hyperz’ (Bolzonella, Miralles & Pelló, 2000), using the seven passbands described in Section 2 (B, V, I_{775} , z, J, H and K_s) and the GISSEL98 library of Bruzual & Charlot (1993). The code ‘hyperz’ computes the probability of an object being at a given redshift z_{phot} by searching for the best (χ^2) fit to its photometric spectral energy distribution (SED) provided by any of the template spectra available in the library. The redshift which yields the highest probability is known as the ‘hyperz’ primary solution and, in the following, we refer to the best-fit SED as the one corresponding to this solution. Although this primary solution is the one used in most cases, ‘hyperz’ also allows one to construct a probability density distribution in redshift space for each object. This is very useful for revealing possible degeneracies in the redshift determination, and for assessing the significance of the primary solution. To account for dust obscuration, we applied a Calzetti et al. (2000) reddening law, allowing the extinction in the V-band (A_V) to vary between 0 and 1. For the reddest objects, we ran ‘hyperz’ again allowing A_V to vary between 0 and 3. This did not produce any substantial changes in the redshift estimations, but does have some impact on the estimated absolute magnitudes and ages.

We also used the public ‘Bayesian photometric redshifts’ (BPZ) code produced by Benítez (2000) to obtain a second, independent set of redshift estimates for the ERGs in our sample. This code computes photometric redshifts using a Bayesian approach (and also has the option of using a maximum likelihood technique like the one used by ‘hyperz’). The agreement between the redshifts estimated by ‘hyperz’ and the BPZ code is very good in most cases. Accordingly, with a few exceptions discussed individually in later sections, we have adopted the ‘hyperz’ results for the ERG sample simply because it provides not only the redshift probability distribution, but also several other useful quantities in the output (e.g. k-corrected absolute magnitudes in a selected filter, V-band dust extinction and age).

Figure 2 shows examples of the best-fit SEDs (left-hand panels) and redshift probability density distributions (right-hand panels) for three of the ERGs in our sample. In the SED plots, the circles correspond to the measured aperture magnitudes in each filter. The solid-line curves indicate the best-fit templates. The SED shown in fig. 2-a) corresponds to an object with ‘hyperz’ primary solution $z_{\text{phot}} = 1.40$. The accuracy in the fitting and the small error bars in the photometry are reflected in a relatively small uncertainty in

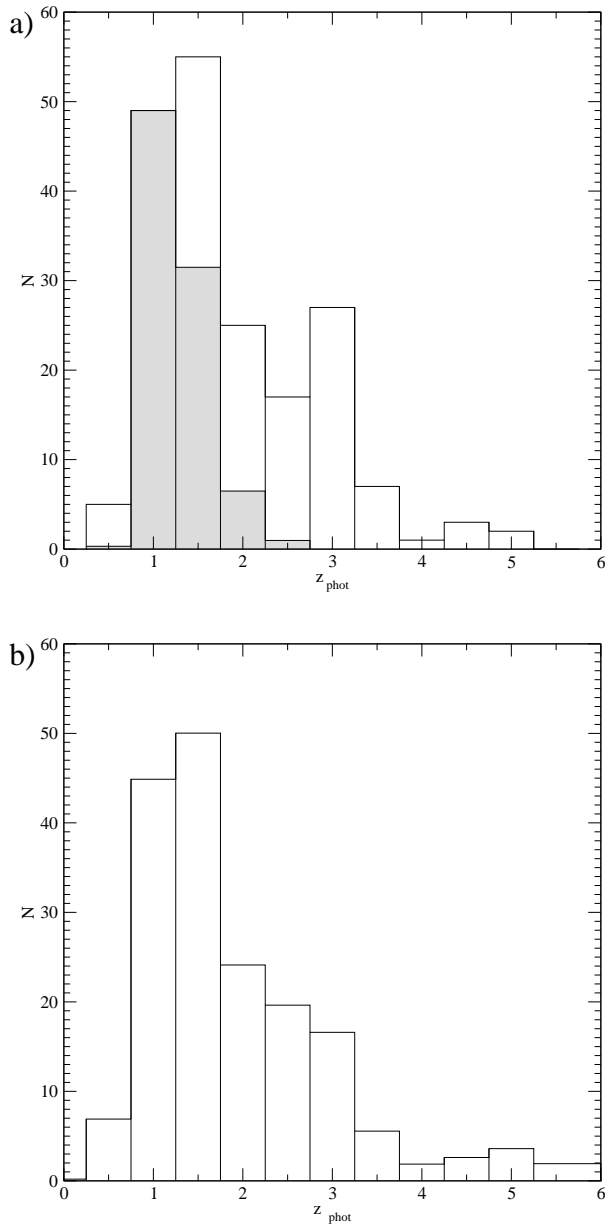


Figure 3. Redshift distribution of the ERGs in Roche et al.’s sample: a) taking into account only ‘hyperz’ primary solutions, b) taking into account the probability density distribution of each ERG in the redshift space. In the upper plot a), the redshift distribution of the shallower sample of ERGs selected by Moustakas et al. (2003) in a wider area of the GOODS/CDFS has been added for comparison (shaded histogram), after division by a factor of 3.08 in order to normalise their distribution to produce the same number of objects in the redshift bin centred at $z_{\text{phot}} = 1$ as found in the present study.

the redshift estimation. The SED shown in fig. 2-b) corresponds to an object with primary solution $z_{\text{phot}} = 2.52$. In this case, the larger error bars in the photometry produce a wider redshift probability density distribution. Finally, the SED in fig. 2-c) corresponds to an ERG with primary solution $z_{\text{phot}} = 5.07$. This is an example of an object with significant degeneracy in redshift space: the corresponding

redshift distribution shows non-negligible probabilities for this object to be either at $z_{\text{phot}} \sim 1$ or $z_{\text{phot}} > 5$.

4 RESULTS

4.1 The redshift distribution

Figure 3 shows our derived redshift distribution for Roche et al. sample of ERGs. A few objects have been excluded either because their light is contaminated by bright neighbours or because they are quite likely to be stars given their very blue ($J - K_s$) colours. These objects are characterised by very low probabilities of being at any redshift as deduced by ‘hyperz’. We constructed the histogram in fig. 3-a) taking into account ‘hyperz’ primary solutions only, for ease of comparison with the Hubble diagrams shown in Section 4.2. For the ERGs with identification numbers e1504 and e1605 in the Roche et al. sample, we adopted the redshifts estimated by the BPZ code by Benítez (2000) instead of the ‘hyperz’ primary solution for reasons which are explained in Section 4.6. We also show the redshift distribution for the shallower sample of ERGs in the HST-ACS field of the GOODS/CDFS obtained by Moustakas et al. (2003) (shaded histogram in fig. 3-a)), after division by a factor of 3.08 in order to normalise their distribution to produce the same number of objects in the redshift bin centred at $z_{\text{phot}} = 1$ as found in the present study.

The redshift distribution for the Roche et al. sample spans the range $z_{\text{phot}} \sim 0.5 - 5.25$. Moustakas et al.’s sample, which is approximately two magnitudes shallower, only includes objects up to redshift $z_{\text{phot}} = 2.5$. The maximum of our redshift distribution of $K_s < 22$ ERGs is located at redshift $z_{\text{phot}} \sim 1.5$. We find a secondary maximum at redshift $z_{\text{phot}} \sim 3$. However, this secondary peak is not statistically significant and disappears when probability densities are used to construct the redshift distribution as shown in fig. 3-b). This latter histogram should be taken as a more realistic representation of the redshift distribution of the ERGs in the Roche et al. sample.

4.2 The Hubble diagram: K_s vs. z_{phot}

Figure 4 shows the Hubble diagram (K_s vs. z_{phot}) for the ERGs in the Roche et al. sample, corresponding to the redshift distribution presented in fig. 3. The plots labelled as a) and b) show the raw and dust-corrected K_s magnitudes as a function of redshift, respectively. We computed the dust-corrected K_s magnitudes using the V-band extinction value A_V applied to the best-fit SED in ‘hyperz’. The rest-frame wavelength sampled by the K_s -band is

$$\lambda_{\text{rf}} = \frac{\lambda_{K_s}}{1 + z_{\text{phot}}}, \quad (1)$$

where λ_{K_s} is the effective wavelength of the K_s filter, i.e. $\lambda_{K_s} = 2.16 \mu\text{m}$. The extinction at a wavelength λ_{rf} is related to the extinction in the V-band (A_V) by

$$A_{\lambda_{\text{rf}}} = \frac{k(\lambda_{\text{rf}}) A_V}{R_V}. \quad (2)$$

For the Calzetti et al.’s (2000) reddening law, $R_V = 4.05 \pm 0.80$ and $k(\lambda_{\text{rf}})$ is a power law in λ_{rf} (cf. ‘hyperz’ user’s

manual). The dust-corrected K_s magnitude for each source is given by the difference ($K_s - A_{\lambda_{\text{rf}}}$).

In both plots 4-a) and 4-b), the circles indicate ‘hyperz’ primary solutions. The error bars correspond to 1σ confidence levels. The overlaid solid curve shows the empirical K_s -z relation fitted for massive radio galaxies (Willott et al. 2003), which approximately corresponds to the locus of passively evolving present-day $3L^*$ galaxies formed instantaneously at redshift $z_f = 10$. The dotted line is a nominal extrapolation of the same law. In fig. 4-a), we have used a dashed line to indicate the region of the Hubble diagram to which the surveys limited at $K_s = 20$ have access. Up to such a magnitude, only sources with $z_{\text{phot}} < 3$ are detected within our survey. For a limiting magnitude $K_s = 22$, the ERGs span the redshift interval $z_{\text{phot}} \sim 0.5 - 5$ and display a large dispersion in the K_s vs. z_{phot} relation. In the raw K_s -magnitude Hubble diagram there is an obvious lack of objects near the radio-galaxy locus beyond redshift $z_{\text{phot}} \sim 3$. However, comparison with fig. 4-b) shows that this effect is a consequence of the presence of dust, rather than indicating a real absence of intrinsically bright, high-redshift ERGs.

The position of a galaxy in the dust-corrected $K_s - z_{\text{phot}}$ diagram depends, of course, on its age as well as its mass. The radio-galaxy K_s -z relation can be interpreted as indicating the behaviour of the highest mass galaxies formed at very high redshift. However, galaxies may appear to be as bright or brighter than high-redshift radio galaxies without being as massive provided their stellar populations are sufficiently young and bright. However, as we show in Section 4.5, most of the galaxies around the radio-galaxy line do in fact appear to at least be massive enough to be the already assembled progenitors of the local $L > L^*$ population. The comparison of fig. 4-a) and 4-b) also shows that the dispersion in the $K_s - z_{\text{phot}}$ relation for ERGs is not an effect produced by the presence of different amounts of dust. We see an even larger dispersion for the ERGs in the dust-corrected Hubble diagram. This fact indicates that the ERG population comprises objects spanning a wide range in mass.

To obtain an estimate of the minimum mass of each ERG, we used the ($k + e$)-corrected K_s -band absolute magnitude of each source and computed a lower limit for the luminosity the galaxy would have at redshift $z = 0$, assuming passive evolution. We explain the details of the calculation of the ($k + e$)-corrected K_s -band absolute magnitudes in Section 4.5. The luminosity L and the absolute magnitude M in a given band are related by the relation $L/L^* = 10^{-0.4(M - M^*)}$, where we considered $M_{K_s}^* = -24.2$ for $h=0.7$, from the 2dF local luminosity function (Cole et al. 2001). Although the exact mass-to-light ratio depends on the assumed initial mass function (IMF) and the age of each galaxy, we estimate the mass of each ERG as $(L/L^*) \times 10^{11} M_\odot$, where L is the luminosity the galaxy would have today at redshift $z = 0$. Estimating the masses in this way, we find that the ERGs in the Roche et al. sample span two decades in mass, from $\sim 3 \times 10^9 M_\odot$ to $\sim 3 \times 10^{11} M_\odot$.

4.3 The red envelope of galaxy evolution

Figures 5-a) and 5-b) show the ($J - K_s$) and ($I_{775} - K_s$) colours, respectively, as a function of photometric redshift for the ERGs in the Roche et al. sample. Only ‘hyperz’ primary solutions are considered in this case. In fig. 5-a),

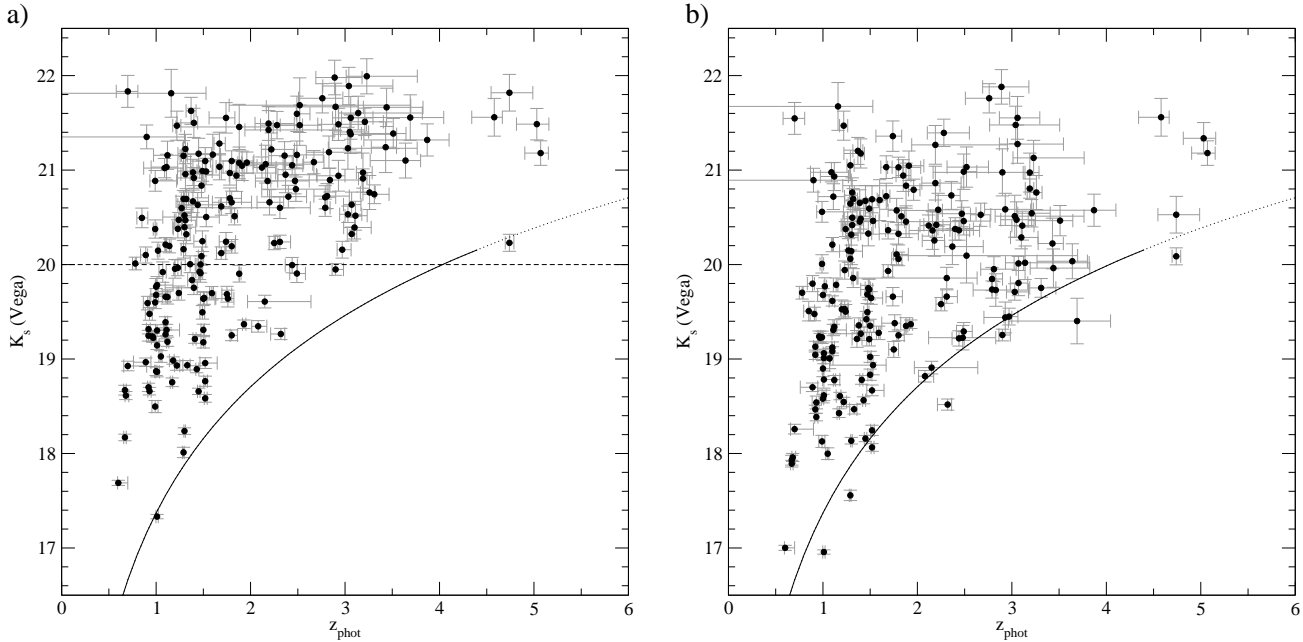


Figure 4. Hubble diagram (K_s magnitude versus photometric redshifts) for the ERGs in the Roche et al. sample. a) Original K_s magnitudes; b) dust-corrected K_s magnitudes. The circles correspond to ‘hyperz’ primary solutions. The error bars indicate 1σ confidence levels. The dashed line on a) delimits the region of the Hubble diagram to which $K_s = 20$ surveys have access. The filled curve corresponds to the empirical K - z relation for massive radio galaxies obtained by Willott et al. (2003), which approximately corresponds to the passive evolution of a $3L^*$ starburst formed at redshift $z_f = 10$. The dotted line is a nominal extrapolation of the same law.

the filled circles correspond to those objects with J-band 2''-diameter aperture magnitude above the 2σ -confidence limit, in this case $J \leq J_{\text{lim.}} = 23.5$ (Vega). The up-triangles indicate lower limits to the colours of those objects with $J > 23.5$, computed as $(23.5 - K_s)$. In fig. 5-b), the mixture of techniques we applied to measure aperture magnitudes on ACS images, i.e. ‘SExtractor’ plus IRAF ‘phot’, does not allow us to set the 2σ confidence limit at a given I_{775} -band magnitude. Thus, we considered as precise colours (filled circles) those with I_{775} -band magnitude error $\varepsilon < 0.5$. For objects with I_{775} -band magnitude error $\varepsilon > 0.5$ we computed lower limits for the colours as $(I_{775} - \varepsilon - K_s)$ (up-triangles). For comparison, we have added in both plots, 5-a) and 5-b), the colours of the three massive galaxies in the HDFS at redshift $z_{\text{phot}} \geq 2.4$, reported by Saracco et al. (2003) (open circles).

The extremely red colours observed in ERGs are due to two coupled factors: age and dust. As our aim is to study which evolutionary model produces the reddest colours observed in the ERGs, we need to correct for the dust effects in order to separate the contribution to the red colours of the evolved stellar populations. Figures 6-a) and 6-b) show the dust-corrected ($J - K_s$) and ($I_{775} - K_s$) colours, respectively, as a function of redshift. We computed the dust-corrections for the colours subtracting from each magnitude the corresponding extinction value given by eq. (2). The symbol labels in both plots of fig. 6 are equivalent to those in fig. 5. We used the public code ‘GALAXEV’ (Bruzual and Charlot 2003) to compute the expected ($J - K_s$) and ($I_{775} - K_s$) colours of different kinds of dust-free passively evolving galaxies, in order to obtain a suitable model for the red envelope delimited by the ERG largest colours. We

found that an instantaneous starburst at redshift $z_f = 5$ with passive evolution thereafter and solar metallicity (solid lines in fig. 6) models quite well the dust-corrected red envelope. A similar starburst formed at redshift $z_f = 5$, but with a higher metallicity $Z = 2.5 Z_\odot$ (dashed line), has been added for comparison. The plots in fig. 6 show that solar metallicity $Z = Z_\odot$ is sufficient to explain the reddest colours observed. Even the few apparent outliers at redshift $z_{\text{phot}} \sim 0.5 - 2.0$ can be explained by such a model once the error bars are taken into account, which are ~ 0.2 mag for these objects. The comparison of fig. 5 and fig. 6 provides a simple and useful way to understand the extent to which the presence of dust is responsible for the original extremely red colours of ERGs.

4.4 The evolving luminosity function of ERGs

Figures 7 and 8 show the luminosity function (LF) of the ERGs in Roche et al.’s sample in different redshift intervals. We assigned to each object the K_s -band k-corrected absolute magnitude (M_{K_s}) obtained as part of the ‘hyperz’ output. We consider ‘hyperz’ primary solutions for binning the data in redshift space. We computed the comoving densities per absolute magnitude bin by dividing the number of sources in each bin by the corresponding comoving volume. To take into account the limits of the survey ($K_s = 22$), we corrected the contribution of each source by a weighting factor $V_{\text{maxbin}}/V_{\text{maxobs}}$, where V_{maxbin} is the volume determined by the maximum redshift of the bin and V_{maxobs} is the volume corresponding to the maximum redshift at which the

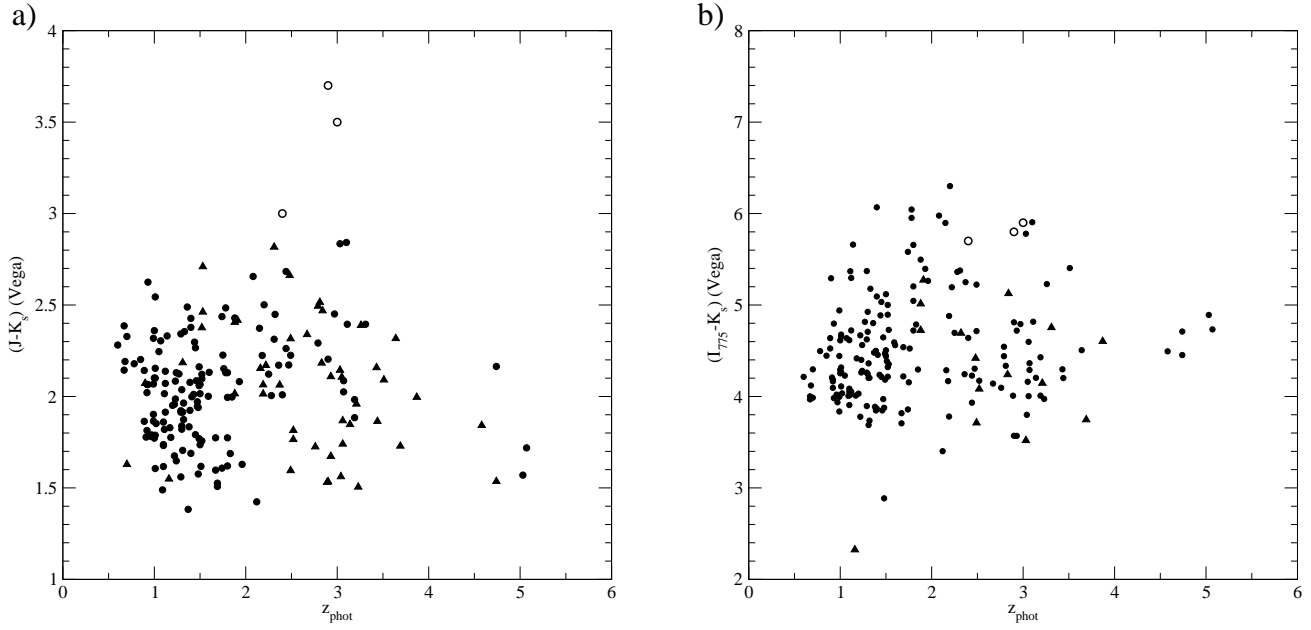


Figure 5. $(J - K_s)$ (a) and $(I_{775} - K_s)$ colours (b) vs. photometric redshifts. The filled circles correspond to exact values and the filled up-triangles, to lower limits for the sources with error $\varepsilon > 0.5$ in the J or I_{775} aperture magnitudes. The open circles indicate the colours of the three high redshift massive galaxies in the HDFS reported by Saracco et al. (2003).

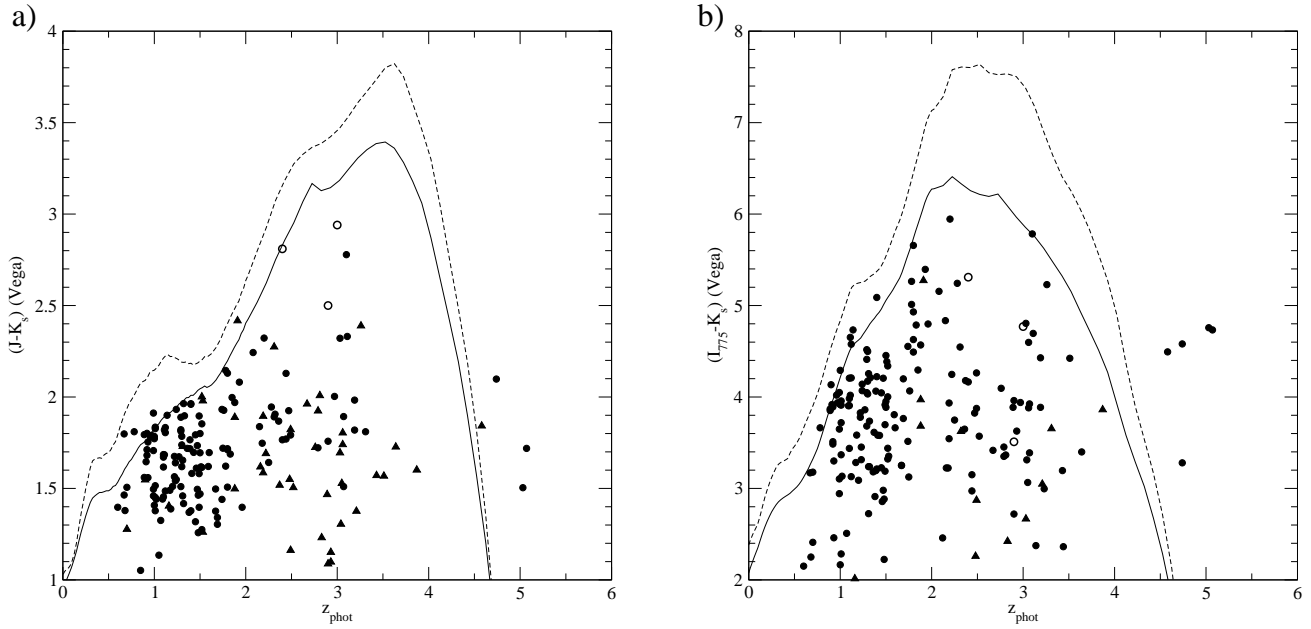


Figure 6. Dust-corrected $(J - K_s)$ (a) and $(I_{775} - K_s)$ colours (b) vs. photometric redshifts. The labels for the filled circles, filled up-triangles and open circles are the same as in fig. 5. The solid line shows the expected colours for a starburst at redshift $z_f = 5$ with passive evolution thereafter and metallicity $Z = Z_\odot$. The dashed line corresponds to the same starburst, but with a higher metallicity $Z = 2.5 Z_\odot$.

source would still be included in the survey (provided it is lower than the maximum redshift of the bin).

Fig. 7 shows the ERG LF at redshifts $\langle z_{\text{phot}} \rangle = 1.0$, $\langle z_{\text{phot}} \rangle = 1.5$ and $\langle z_{\text{phot}} \rangle = 2.0$, indicated by circles, squares and up-triangles, respectively. The error bars correspond to the maximum of the Poissonian errors and the errors due

to cosmic variance, which we take on average as 40% in the number counts at these redshifts (cf. Somerville et al. 2003). The inclusion of the cosmic variance is fundamental for highly-clustered populations, as ERGs at redshifts $z \sim 1 - 2$ are known to be. The global K_s -band LF at redshifts $1 < z_{\text{phot}} < 2$ has been added for comparison.

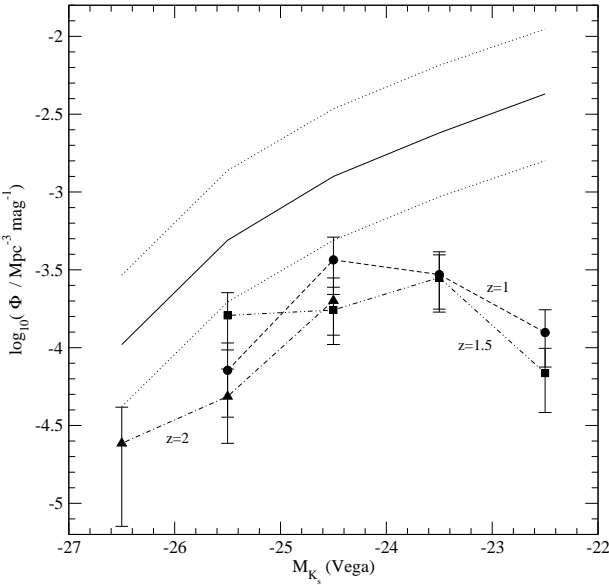


Figure 7. Luminosity function of ERGs at different redshifts: $\langle z_{\text{phot}} \rangle = 1.0$ (circles), $\langle z_{\text{phot}} \rangle = 1.5$ (squares) and $\langle z_{\text{phot}} \rangle = 2.0$ (up-triangles). The average global K_s -band LF in the HDFN and HDFS has been overlaid for comparison (solid line). The latter has been computed integrating in each absolute magnitude bin the Schechter functions fitted by Bolzonella et al. (2002) in these fields. The error bars have been estimated using the maximum uncertainty in the normalisation parameter ϕ^* , obtained for the HDFS (dotted lines).

The solid line represents the average K_s -band LF of the HDFS and HDFN, obtained by integrating in each absolute magnitude bin the best Schechter function fitted by Bolzonella, Pelló & Maccagni (2002) for datasets in these fields up to a limiting magnitude of $K_s \sim 23$. The dotted lines indicate the largest error bars in the normalisation parameter ϕ^* , corresponding to the fitting of the HDFS data. As expected, our ERG LF reproduces the shape of the bright end of the global K_s -band LF. The differences at fainter magnitudes are at least in part due to the nature of the ERG colour selection. We find only 3 very luminous galaxies with $-27 < M_{K_s} < -26$ with estimated redshifts $z_{\text{phot}} \in [0.75; 2.25]$, 2 of which have redshifts in the interval $[1.75; 2.25]$. These 2 sources have $(I_{775} - K_s) \geq 5.9$ and $(J - K_s) > 2.3$. For the absolute magnitude range $-26 < M_{K_s} < -24$, we do not observe any evolution in the ERG LF from redshifts $\langle z_{\text{phot}} \rangle = 1.0$ to $\langle z_{\text{phot}} \rangle = 2.0$. Any fluctuation in the mean values of the LF in this absolute magnitude bin can be accounted for within the cosmic variance error bars. For absolute magnitudes $-24 < M_{K_s}$ we do not observe any evolution in the LF from redshifts $\langle z_{\text{phot}} \rangle = 1.0$ to $\langle z_{\text{phot}} \rangle = 1.5$. The limits of the survey (which is considered to be complete up to $K_s = 21.5$) do not allow us to explore the LF at redshift $\langle z_{\text{phot}} \rangle = 2.0$ for such faint objects.

In figure 8, we show again the ERG LF at redshifts $\langle z_{\text{phot}} \rangle = 1.0, 1.5, 2.0$ and we add the ERG LF at $\langle z_{\text{phot}} \rangle = 2.5$, for comparison. We computed the latter taking into account all the objects in the redshift interval $[2.0, 3.0]$. At

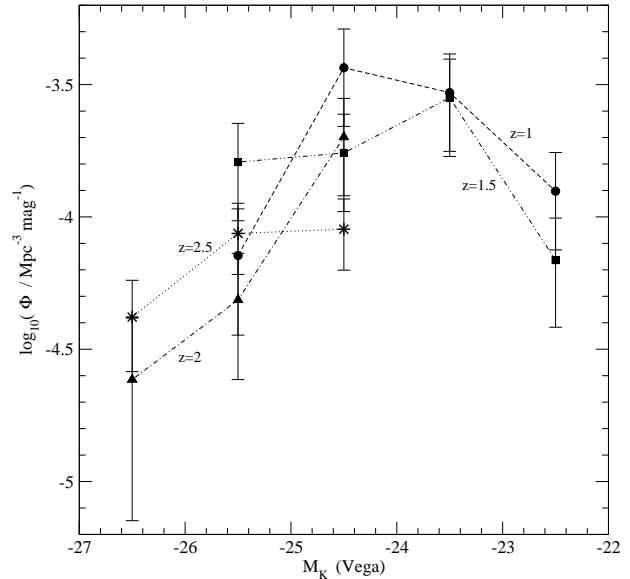


Figure 8. Luminosity function of ERGs at different redshifts. The references are the same as in fig. 7. The LF at redshifts $2 < z_{\text{phot}} < 3$ has been added (star-like symbols). This plot shows that the bright end of the ERG LF does not obviously decrease from redshifts $\langle z_{\text{phot}} \rangle = 2.0$ to $\langle z_{\text{phot}} \rangle = 2.5$.

these redshifts, we have adopted a slightly lower value for the typical cosmic variance, only 30% in the number of counts on average (Somerville et al. 2003). This plot shows that the bright end of the ERG LF does not decrease significantly from redshifts $\langle z_{\text{phot}} \rangle = 2.0$ to $\langle z_{\text{phot}} \rangle = 2.5$. This result confirms the existence of a population of extremely red bright galaxies at high redshifts. We find 7 objects with estimated redshifts $\langle z_{\text{phot}} \rangle = 2.0$ to $\langle z_{\text{phot}} \rangle = 2.5$ and absolute magnitudes $-27 < M_{K_s} < -26$, 6 of which have $(I_{775} - K_s) \geq 4.8$, placing them among the very reddest objects at these redshifts. Moreover, all of these objects have $(J - K_s) \geq 2.2$. In the next section we investigate the change of the absolute magnitudes of ERGs after evolution to redshift $z = 0$ and explore the comoving densities of potential progenitors of the local $L > L^*$ population.

4.5 Comoving densities of massive galaxies

In this section we study the comoving densities of ERGs that will still contribute to the bright end of the K_s -band LF once they evolve down to redshift $z = 0$. If we assume passive evolution for ERGs from the epoch of observation, the maximum dimming of the absolute magnitude M_{K_s} can be estimated and, thus, a lower limit to the luminosity each object would have at redshift $z=0$ obtained. To do this, we need to estimate an evolutionary correction (e-correction) factor at redshift $z = 0$ which, when added to the ‘hyperz’ k-corrected absolute magnitude, yields the absolute magnitude the galaxy would have today. The e-correction for each galaxy depends on its spectral type and age. We used the public code ‘GALAXEV’ (Bruzual and Charlot 2003) to compute the absolute magnitudes at redshift $z = 0$ of the spectral types corresponding to our ERGs at different ages.

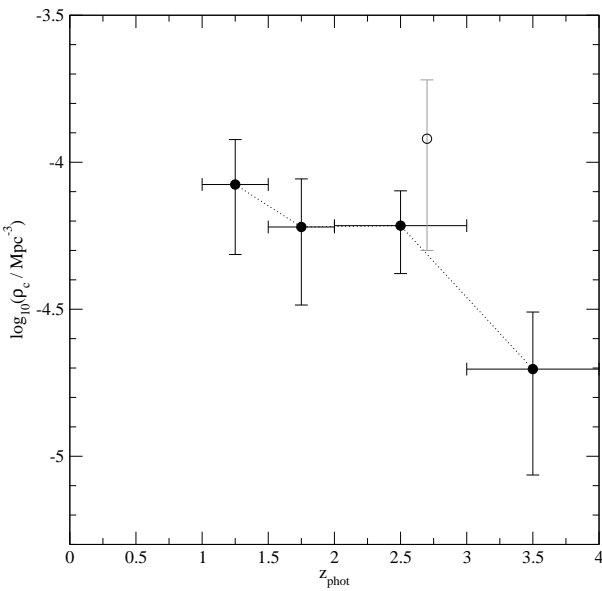


Figure 9. Lower limits on the comoving densities of passively evolving $L > L^*$ ERGs (filled circles) as a function of redshift. The horizontal error bars indicate the binning in the redshift space. The vertical error bars correspond to Poissonian errors in the number of objects. The lower limit on the comoving density of progenitors of $L > L^*$ galaxies at redshift $\langle z_{\text{phot}} \rangle = 2.7$ obtained by Saracco et al. (2003) has been added for comparison (open circle).

The correction applied to each object is the difference in the absolute magnitude the object would have today and at the age it had when its light was emitted. The objects that are considered to be progenitors of the local $L > L^*$ population are those with $(k + e)$ -corrected absolute magnitude $M_{K_s} < M_{K_s}^*$, given the relationship $L/L^* = 10^{-0.4(M - M^*)}$. In a passive evolution scenario, these ERGs must have contained a minimum stellar mass of $\sim 10^{11} M_\odot$ when their light was emitted.

Figure 9 shows the comoving densities at different redshifts of the 27 ERGs in Roche et al.'s sample which are expected to have $L > L^*$ at redshift $z = 0$ under passive evolution. We used $M_{K_s}^* = -24.2$ for $h=0.7$ (Cole et al. 2001). Once more, we computed the comoving densities dividing the number of sources in each redshift bin by the corresponding comoving volume. We divided the sample in bins of width $\Delta z_{\text{phot}} = 0.5$ up to redshift $z_{\text{phot}} = 2$ and $\Delta z_{\text{phot}} = 1$ for redshifts $2 < z_{\text{phot}} < 4$. To compute these comoving densities, we did not use 'hyperz' primary solutions but a redshift probability density distribution that we constructed normalising for each source the percentage probabilities given in the 'hyperz' output file `log.phot`. In this way, each source may contribute in a fraction to different redshift bins. Only sources with 'hyperz' primary solutions $z_{\text{phot}} < 4$ have been taken into account. We applied a weighting factor of the kind $V_{\text{maxbin}}/V_{\text{maxobs}}$, as it was explained in Section 4.4, to the normalised probability density distribution of each source. However, in each case, the weighting factor has been estimated using only the k -corrected absolute magnitude M_{K_s} given by 'hyperz' in the output. A

more rigorous procedure should take into account a probability density distribution for the absolute magnitudes in correspondence with the probability density distribution for redshifts. The error bars for the comoving densities correspond to Poissonian errors in the number of sources, which are dominant in this case.

Our results show that there is no significant change in the comoving densities of ERG progenitors of $L > L^*$ galaxies between redshifts $1.5 < z_{\text{phot}} < 2.0$ and $2 < z_{\text{phot}} < 3$, which is consistent with the results presented in Section 4.3 for the bright end of the LF. Actually, all the galaxies with $-27 < M_{K_s} < -26$ in Section 4.3 are included in the progenitors of $L > L^*(z = 0)$ subsample. This lack of variation in the comoving densities of massive ERGs is in disagreement with the predictions of semianalytic models (Kauffmann and Charlot 1998, Moustakas & Somerville 2002). The values we obtain for the comoving densities are: $\rho_c = (8.4 \pm 3.5) \times 10^{-5} \text{ Mpc}^{-3}$ for $\langle z_{\text{phot}} \rangle = 1.25$, $\rho_c = (6.0 \pm 2.7) \times 10^{-5} \text{ Mpc}^{-3}$ for $\langle z_{\text{phot}} \rangle = 1.75$ and $\rho_c = (6.0 \pm 1.9) \times 10^{-5} \text{ Mpc}^{-3}$ for $\langle z_{\text{phot}} \rangle = 2.5$. It is important to note that the relatively small comoving densities at $\langle z_{\text{phot}} \rangle = 1.25$ and $\langle z_{\text{phot}} \rangle = 1.75$ are expected to be due to the ERG colour cutoff. Although the ERGs reproduce quite well the shape of the bright end of the global K_s -band LF, the values are lower, indicating that larger comoving densities of massive objects are expected to be obtained in a K_s -selected sample without a colour selection. Thus, the conclusion of a constant comoving density of massive objects from redshifts $1.5 < z_{\text{phot}} < 2.0$ and $2 < z_{\text{phot}} < 3$ is in principle only applicable to ERGs, and may of course not hold for a general K_s -selected sample. The mean value we obtain for the lower limit to the comoving density of $L > L^*$ progenitors at $\langle z_{\text{phot}} \rangle = 2.5$ is only one half of the mean value obtained by Saracco et al. (2003b) at a similar redshift (open circle in fig. 9), but there is no significant discrepancy between the results given the large error bars. We conclude that Saracco et al.'s large mean comoving density might be due to a simple cosmic variance effect and much larger samples of K_s -selected galaxies are necessary to establish a robust estimate of the fraction of the stellar mass already assembled in ERGs at these redshifts.

Interestingly, the progenitors of $L > L^*$ galaxies are among the reddest ERGs. At different redshifts, these massive galaxies in the Roche et al. sample have $\langle (I_{775} - K_s) \rangle \approx 4.8 - 5.1$. The mean $(J - K_s)$ colours increase with redshift, as it is expected when the 4000Å break enters the region between the J and K_s filters. In all cases, $(J - K_s) > 2$. Some of these massive galaxies are among the reddest objects in $(J - K_s)$ at redshifts $z_{\text{phot}} > 2$, due to the combined effects of the break and considerable amounts of dust (we find V -band extinction values of up to $A_V = 1.8$ for these massive objects). However, not all the $(J - K_s)$ reddest objects evolve to $L > L^*$ sources in a passive evolution scenario. In some cases, the extremely red $(J - K_s)$ colours are almost exclusively due to very large dust extinctions. The characteristics of these sources are consistent with the 'hyper extremely red object' population discovered by Totani et al. (2001). Recently, some extremely red $(J - K_s)$ sources have been found to be counterparts of sub-millimetre sources. However it is not yet clear whether the ERGs associated with sub-millimetre sources are primarily high or low mass objects (Frayer et al. 2003).

4.6 Sources beyond redshift $z = 4$ - the ERG - Lyman-break connection

In this section we focus on the properties of the Lyman-break galaxies in the GOODS/CDFS included in the Roche et al. ERG sample. These objects are candidates for massive galaxies at very high redshift. Here we summarise the detailed properties of the individual objects and discuss the probability that they are genuinely located at such high redshifts.

Several studies have already been published on the selection of very high redshift candidate sources in the GOODS fields (Stanway, Bunker & McMahon 2003; Bouwens et al. 2003; Bremer et al. 2004; Dickinson et al. 2003b). In most of these studies a colour cutoff selection technique has been applied (usually $(I_{775} - z) > 1.3 - 1.5$, AB) to select candidates at redshifts $z > 5$. We find some of these candidate sources in the Roche et al. ERG sample. Our estimated redshifts confirm one of these common sources as being at $z_{\text{phot}} > 5$, while all the others appear as lower redshift sources. We argue that the fraction of low-mass star and lower-redshift ERG contaminants is usually under-estimated when a single-colour selection criterion is applied. Multicolour photometry appears to be a much more powerful way to obtain reliable candidate lists of very high redshift objects, and allows the investigation of degenerate solutions in redshift space.

We find 5 ERGs with ‘reliable’ estimated redshifts $z_{\text{phot}} > 4$ in the Roche et al. sample. The initial ‘hyperz’ output list contained 12 sources with a primary solution at $z_{\text{phot}} > 4$, which adopted as candidates for detailed inspection. We present the properties of the complete list of 12 candidate sources in Table 1. We used the public code BPZ (Benítez 2000) to obtain estimated redshifts for these objects in an independent way. We also made an individual study of each of our 12 candidate sources, inspecting their ACS images and analysing their magnitudes and colours in different bands. We rejected the following 7/12 $z > 4$ candidates for the reasons explained below:

- **e114-e566-e967-e2386** : these sources appear to be at redshifts $z_{\text{phot}} > 5.3$ from ‘hyperz’ and all of them have $(I_{775} - z) \sim 1.3 - 1.5$, AB. Only e566 is not confirmed by the BPZ code as a very high redshift source (it is estimated to be at redshift $z_{\text{phot}} = 1.28$). However, the probabilities associated with the ‘hyperz’ primary solutions, obtained from the χ^2 minimisation, are very low ($P < 19\%$) in all cases. e967 corresponds to source number 4 in Stanway et al. list and source number 8 in the list of Bremer et al. e114 and e2386 are sources number 13 and 9 in the Bremer et al. list, respectively. These sources are unresolved on ACS images and have quite blue near-IR colours, $(J - K_s) < 1.7$ (Vega) in all cases. e967 and e2386 are significant detections in the V-band ($V = 27.9 \pm 0.4$ and $V = 27.4 \pm 0.3$, AB, respectively) and e566, in the B-band ($B = 23.7 \pm 0.1$, AB). Thus, it is more likely that they are cool stars than high redshift galaxies. Indeed, e967 has been spectroscopically confirmed as such (cf. Dickinson et al. 2003b). These cool stars are known to be among the main contaminants of very high redshift candidates.

- **e1504**: this source has ‘hyperz’ primary solution

$z_{\text{phot}} = 4.63$, but actually has a probability $P \equiv 0$ at any redshift between 0 and 10. The BPZ code gives an estimated redshift of $z_{\text{phot}} = 1.44$ for this source. Besides, although it is not detected in the V-band¹, it is a significant detection in the B-band ($B = 27.2 \pm 0.3$, AB).

- **e1605**: this source has ‘hyperz’ primary solution $z_{\text{phot}} = 6.71$ (with an associated probability $P \approx 90\%$), but the BPZ code gives $z_{\text{phot}} = 2.84$. This source is not detected on the z-band images, but it could have some flux in the I_{775} -band ($I_{775} = 27.9 \pm 1.3$, AB). Its very red near-IR colour, i.e. $(J - K_s) > 2.5$ (Vega), suggests that the estimated redshift from the BPZ code is more reliable in this case.

- **e2006**: this source has two ‘hyperz’ solutions with similar probabilities. The primary solution is $z_{\text{phot}} = 6.21$ ($P \approx 73\%$) and the secondary one is $z_{\text{phot}} = 1.15$ ($P \approx 60\%$). The BPZ estimation is $z_{\text{phot}} = 6.37$. We measured $(I_{775} - z) = 2.1 \pm 0.8$ for this object and we do not find it is significantly detected in either the B or V bands. However, the higher redshift solution would imply it is an extremely bright galaxy with a k-corrected absolute magnitude $M_{K_s} = -28.5$ and estimated mass $\sim 6.7 \times 10^{11} M_\odot$, so we consider that in this case the ‘hyperz’ secondary solution is more likely to be the right answer.

Our 5/12 accepted $z > 4$ candidates, whose redshift probability density distributions we show in fig. 10, are the following:

- **e491**: ‘hyperz’ primary solution is $z_{\text{phot}} = 4.58$ (with an associated probability $P \approx 98\%$). The BPZ code estimates a redshift of $z_{\text{phot}} = 5.22$. There are no significant secondary solutions for the redshift of this source in ‘hyperz’. The K_s -band k-corrected absolute magnitude for this galaxy is $M_{K_s} = -25.6$ and we estimate a mass of $5.8 \times 10^{10} M_\odot$. This object has $(I_{775} - z) = 0.6 \pm 0.3$ and it is not detected in either the B or V bands.

- **e778**: ‘hyperz’ primary solution is $z_{\text{phot}} = 4.74$ (with an associated probability $P \approx 98\%$). The BPZ redshift estimation is $z_{\text{phot}} = 5.42$. However, this source has a non-negligible probability of being at redshift $z_{\text{phot}} = 3.26$ ($P \approx 39\%$). The K_s -band k-corrected absolute magnitude for this galaxy is $M_{K_s} = -26.4$, with estimated mass $1.1 \times 10^{11} M_\odot$. We do not detect this object in either the B or V bands. This source is included in the list of 100 reddest sources of the GOODS/CDFS Ultra-Deep Field (UDF) and has a colour $0.9 < (I_{775} - z) < 1.5$. The improved photometry available following the release of the UDF data will allow the redshift of this source to be determined more accurately.

- **e1113**: this source has a ‘hyperz’ primary solution $z_{\text{phot}} = 5.07$ ($P \approx 56\%$) and secondary solution $z_{\text{phot}} = 1.10$ ($P \approx 26\%$). The BPZ code favours a low redshift solution $z_{\text{phot}} = 1.05$. The estimated K_s -band k-corrected absolute magnitude for this galaxy is $M_{K_s} = -26.9$. Thus, if this galaxy is at $z_{\text{phot}} \sim 5$, it will be a very massive object of $1.8 \times 10^{11} M_\odot$. We measured $(I_{775} - z) = 1.4 \pm 0.2$ and we do not detect the source in either the B or V bands. This source corresponds to object number 2 in Stanway et al.’s list. We

¹ even when its flux is manually measured with the IRAF task ‘phot’

Table 1. List of ERGs in the Roche et al. sample with ‘hyperz’ primary solutions $z_{\text{phot}} > 4$. The first column is the identification number. The second and third columns indicate the coordinates of the source obtained from the K_s -band images. The fourth and fifth columns show the redshifts estimated by ‘hyperz’ and the BPZ code, respectively. Column six lists comments on the individual objects.

ERG id	RA(J2000)	DEC(J2000)	hyperz	BPZ	accepted?	COMMENTS
114	3:32:22.46	-27:50:47.16	$5.60^{+0.03}_{-0.14}$	5.75	N	Unresolved. $(J - K_s)_{\text{Vega}} = 0.8 \pm 0.3$
566	3:32:24.78	-27:49:12.91	$6.69^{+0.11}_{-0.12}$	1.28	N	Unresolved. $(J - K_s)_{\text{Vega}} = 1.1 \pm 0.3$. $BAB = 23.7 \pm 0.1$
967	3:32:18.17	-27:47:46.48	$5.39^{+0.03}_{-0.08}$	5.70	N	Spectroscopically confirmed star. $V_{AB} = 27.9 \pm 0.4$
1504	3:32:18.17	-27:46:16.33	$4.63^{+0.10}_{-0.06}$	1.44	N	$BAB = 27.2 \pm 0.3$
1605	3:32:19.67	-27:46:02.04	$6.71^{+0.75}_{-0.32}$	2.84	N	$(J - K_s)_{\text{Vega}} > 2.5$. Not detected in z band.
2386	3:32:19.23	-27:45:45.39	$5.33^{+0.05}_{-0.04}$	5.56	N	Unresolved. $(J - K_s)_{\text{Vega}} = 1.2 \pm 0.2$
2006	3:32:28.81	-27:44:30.54	$6.21^{+0.17}_{-0.33}$	6.37	N	Redshift $z_{\text{phot}} = 6.21$ would imply $\sim 6.7 \times 10^{11} M_{\odot}$.
491	3:32:25.95	-27:49:30.38	$4.58^{+0.24}_{-0.09}$	5.22	Y	No significant ‘hyperz’ secondary solutions.
778	3:32:41.76	-27:48:24.92	$4.74^{+0.20}_{-0.25}$	5.42	Y	‘hyperz’ secondary solution $z_{\text{phot}} = 3.26$.
1113	3:32:34.65	-27:47:20.89	$5.07^{+0.16}_{-0.08}$	1.05	Y	‘hyperz’ secondary solution $z_{\text{phot}} = 1.10$
1272	3:32:41.69	-27:46:55.40	$5.03^{+0.21}_{-0.13}$	5.48	Y	No significant ‘hyperz’ secondary solutions.
1703	3:32:37:74	-27:45:05.41	$4.74^{+0.04}_{-0.05}$	5.38	Y	No significant ‘hyperz’ secondary solutions.

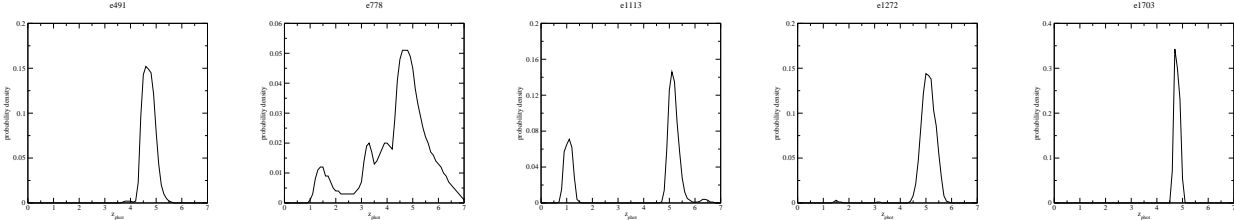


Figure 10. Redshift probability density distributions for the accepted $z > 4$ candidate sources in the Roche et al. ERG sample.

also accept it as a very high redshift candidate but with the warning that it might be a lower redshift contaminant.

• **e1272:** this source has a ‘hyperz’ primary solution $z_{\text{phot}} = 5.03$ ($P \approx 82\%$) and no significant secondary solution. The BPZ estimation is $z_{\text{phot}} = 5.48$. The estimated K_s -band k-corrected absolute magnitude for this source is $M_{K_s} = -26.5$ and the estimated mass is $1.3 \times 10^{11} M_{\odot}$. It has $(I_{775} - z) = 1.2 \pm 0.4$ and no significant detection in the B or V bands.

• **e1703:** this source has a ‘hyperz’ primary solution $z_{\text{phot}} = 4.74$ ($P \approx 90\%$) and no significant secondary solution. The BPZ redshift is $z_{\text{phot}} = 5.38$. The estimated K_s -band k-corrected absolute magnitude for this source is $M_{K_s} = -27.3$ and the estimated mass is $2.7 \times 10^{11} M_{\odot}$. It has $(I_{775} - z) = 0.97 \pm 0.14$ and it is not detected in either the B or V bands.

4/5 of our accepted $z_{\text{phot}} > 4$ candidates have $L > L^*(z = 0)$. The existence of 4 progenitors of local $L > L^*$ galaxies in an area of 50.4 arcmin^2 in the redshift range $[4.5, 5.5]$ would account for a comoving density of $\rho_c \approx (2.9 \pm 1.5) \times 10^{-5} \text{ Mpc}^{-3}$, which is only one half of the values we find for massive ERGs at redshifts $\langle z_{\text{phot}} \rangle = 1.75$ and $\langle z_{\text{phot}} \rangle = 2.5$.

Finally, we list other ERGs in the Roche et al. sample which are among the very-high redshift candidates selected by other authors, and for which we obtain lower redshift estimates:

ERG id	Author	Author’s id	‘hyperz’
82	Bremer et al.	7	$1.40^{+0.30}_{-0.04}$
309	Bremer et al.	6	$2.32^{+0.11}_{-0.05}$
225	Dickinson et al.	SiD013	$1.74^{+0.08}_{-0.10}$
1423	Bremer et al.	2	$1.60^{+0.28}_{-0.08}$

From the sources listed above, only e309 has a very-high-redshift secondary solution, although with negligible significance, at $z_{\text{phot}} = 6.74$.

4.7 Review of the ERG cluster candidate at redshift $z \sim 1.5$

Roche et al. (2003) found 10 ERGs within a $20''$ radius of the Chandra source XID:58 (RA=3:32:11.85, DEC=27:46:29.14), which is itself a counterpart of the ERG identified as e1435 in Roche et al.’s list. This overdensity suggested the presence of an ERG cluster at redshift $z \sim 1.5$, based on the photometric redshift of the Chandra source XID:58, estimated as $z_{\text{phot}} = 1.44$ by Mainieri et al. (in prep.). Based on the source colours, Roche et al. argued that 7/9 of the ERGs around XID:58 (e1435) could be part of that cluster. In the following table, we present our redshift estimates (both primary and secondary) for e1435 and the 7 surrounding sources that could be associated with it.

ERG id	z_{phot} (primary)	z_{phot} (sec.)
1333	$3.10^{+0.11}_{-0.18}$	1.78
1341	$1.52^{+0.06}_{-0.13}$	1.01
1390	$1.29^{+0.01}_{-0.01}$	1.67
1404	$1.52^{+0.02}_{-0.03}$	1.78
1423	$1.60^{+0.28}_{-0.09}$	1.34
1435 (XID:58)	$1.85^{+0.08}_{-0.08}$	1.30
1464	$3.19^{+0.07}_{-0.10}$	1.48
1481	$1.30^{+0.12}_{-0.12}$	1.01

Our estimated redshifts seem to confirm the presence of a cluster at redshift $z_{\text{phot}} \sim 1.5$. However, it is not clear whether all the sources listed above belong to it. e1333 and e1464 seem to be higher redshift sources, although the ‘hyperz’ secondary solution might locate e1464 at redshift $z_{\text{phot}} = 1.48$. For e1435 (counterpart of XID:58) we estimate a redshift $z_{\text{phot}} = 1.85$, a value somewhat higher than Mainieri et al.’s estimation. Our secondary solution, on the contrary, is closer to their value. The sources which seem to be part of a cluster at redshift $z_{\text{phot}} \sim 1.5$ are e1341, e1404, e1423 and e1481.

Roche et al. also suggested that the 2/9 remaining ERGs around XID:58 could be associated with another X-ray source (Chandra XID:149), which is spectroscopically confirmed to be at redshift $z_{\text{phot}} = 1.033$ (Hasinger, private communication). Our estimated redshifts for these 2 remaining ERGs are:

ERG id	z_{phot} (primary)	z_{phot} (sec.)
1311	$1.05^{+0.02}_{-0.02}$	0.61
1467	$1.07^{+0.04}_{-0.04}$	5.24

The ‘hyperz’ primary solutions seem to confirm that these 2 ERGs are actually associated with the X-ray source XID:149.

5 SUMMARY AND CONCLUSIONS

In this paper we have presented estimated redshifts for the Extremely Red Galaxies selected by Roche et al. (2003) in the 50.4 arcmin² of the GOODS/CDFS deep ISAAC field to a limiting magnitude $K_s = 22$. This is the deepest significant sample of ERGs selected to date and constitutes a complement to other shallower but wider surveys of ERGs in the same field (Moustakas et al. 2003).

We have used multicolour photometry in seven passbands (B,V, I₇₇₅, z, J, H and K_s) to compute photometric redshifts using the public code ‘hyperz’. The B,V, I₇₇₅ and z magnitudes have been measured on the stacked 5-epoch GOODS ACS images (v1.0 data release). We have obtained the redshift distribution and the corresponding Hubble diagram ($K_s - z_{\text{phot}}$), which show the existence of ERGs up to redshifts $z_{\text{phot}} \sim 5$ at this depth. The ERG population is characterised by a large dispersion in the $K_s - z_{\text{phot}}$ relation. We find that this dispersion is even more important in the dust-corrected Hubble diagram, indicating that the ERG population is composed of objects spanning a wide

range in mass. We estimate that the ERGs in Roche et al.’s sample span two decades in mass, from $\sim 3 \times 10^9 M_\odot$ to $\sim 3 \times 10^{11} M_\odot$.

We have studied the red envelope of galaxy evolution, determining the galaxy template which best describes the ERG dust-corrected reddest colours observed in the Roche et al. sample as a function of redshift. We find that a starburst formed at redshift $z_f = 5$ with passive evolution thereafter and solar metallicity provides a very good description of the red envelope of ERG evolution for objects selected with $K_s < 22$. Our work indicates that the simplified traditional picture for ERGs as either old elliptical galaxies or young dusty starbursts can no longer be sustained. The colours of many of the reddest ERGs can only be explained by the combined effects of evolved stellar populations and dust.

We have also explored the evolution of the ERG luminosity function from redshifts $\langle z_{\text{phot}} \rangle = 1$ to $\langle z_{\text{phot}} \rangle = 2.5$. The ERG LF at redshifts $1 < z_{\text{phot}} < 2$ reproduces the shape of the bright end of the global K_s -band LF, as perhaps expected. We find no evolution in the bright end of the LF of ERGs from redshifts $\langle z_{\text{phot}} \rangle = 1.0$ to $\langle z_{\text{phot}} \rangle = 2.5$ ($-26 < M_{K_s} < -25$) and from redshift $\langle z_{\text{phot}} \rangle = 2.0$ to $\langle z_{\text{phot}} \rangle = 2.5$ ($-26 < M_{K_s} < -26$). This effect cannot be deduced from inspection of the Hubble diagram for ERGs, constructed using the raw K_s magnitudes. Only after the application of dust corrections are some ERGs revealed as bright and massive galaxies.

A main goal in the selection of ERG samples is to trace the progenitors of very luminous local galaxies ($L > L^*$). We find that only a small fraction ($\sim 15\%$) of the ERGs in the Roche et al. sample can evolve into such luminous galaxies under passive evolution. However, the comoving densities of these ERGs seem to be constant from redshifts $\langle z_{\text{phot}} \rangle = 1.75$ to $\langle z_{\text{phot}} \rangle = 2.5$, reinforcing the idea of the presence of progenitors of local $L > L^*$ galaxies at redshifts $z > 2$.

Finally, we have investigated the existence of Lyman break galaxies massive enough to be included in an ERG sample. We found 5 ERGs with high probabilities of being located at redshifts $z_{\text{phot}} > 4$. 4/5 of these objects are very massive ($> 10^{11} M_\odot$) and could account for a comoving density of progenitors of local $L > L^*$ galaxies of $\rho_c \approx (2.9 \pm 1.5) \times 10^{-5} \text{ Mpc}^{-3}$, which is only one half of the values we find for massive ERGs at redshifts $\langle z_{\text{phot}} \rangle = 1.75$ and $\langle z_{\text{phot}} \rangle = 2.5$. Deep observations in wider areas are crucial in order to better constrain lower limits on the fraction of massive galaxies with the bulk of their stellar mass already assembled at high redshifts.

Several open questions still remain for the ERG population in the GOODS/CDFS field. An important issue is to understand how ERG morphology changes with redshift, a problem we plan to study in a future paper. Also, very deep spectroscopic observations scheduled with the Gemini Multiobject Spectrograph (GMOS) will provide more accurate redshifts for a subset of the ERGs in the Roche et al. sample, allowing a detailed study of their properties.

ACKNOWLEDGEMENTS

This paper is based on observations made with the Advanced Camera for Surveys on board the Hubble Space Telescope

operated by NASA/ESA and with the Infrared Spectrometer and Array Camera on the ‘Antu’ Very Large Telescope operated by the European Southern Observatory in Cerro Paranal, Chile, and form part of the publically available GOODS datasets. We thank the GOODS teams for providing reduced data products.

KIC acknowledges funding from a POE-network studentship and the Overseas Research Scheme Award (ORS/2001014037). JSD, RJM and NDR acknowledge PPARC funding.

REFERENCES

Aretxaga I., Hughes D. H., Chapin E. L., Gaztañaga E., Dunlop J. S., Ivison R. J., 2003, MNRAS, 342, 759

Benítez N., 2000, ApJ, 536, 571

Bertin E., Arnouts S., 1996, A&A, 117, 393

Bolzonella M., Miralles J.-M., Pelló R., 2000, A&A, 363, 476

Bolzonella M., Pelló R., Maccagni D., 2002, A&A, 395, 443

Bouwens R. J., Illingworth G. D., Rosati P., Lidman C. et al., 2003, ApJ, 595, 589 (astro-ph/0306215)

Bremer M.N., Lenhert M.D., Waddington I., Hardcastle M.J., Boyce P.J., Phillipps S., 2004, MNRAS, 346, L7 (astro-ph/0306587)

Bruzual A. G., Charlot S., 1993, ApJ, 405, 538

Bruzual G., Charlot S., 2003, MNRAS, 344, 1000

Calzetti D., Armus L., Bohlin R. C., Kinney A. L., Koornneef J., Storchi-Bergmann T., 2000, ApJ, 533, 682

Chapman S. C., Blain A. W., Ivison R. J., Smail I. R., 2003, Nature, 422, 695

Charlot S., Fall S. M., 2000, ApJ, 539, 718

Cimatti A., Andreani P., Röttgering H., Tilanus R., 1998, Nature, 392, 895

Cimatti A., Daddi E., Mignoli M., Pozzetti L. et al., 2002, A&A, 381, L68

Cole S., Norberg P., Baugh C. M., Frenk C. S. et al., 2001, MNRAS, 326, 255

Dey A., Graham J. R., Ivison R. J., Smail I., Wright G. S., Liu M. C., 1999, ApJ, 519, 610

Dickinson M., Giavalisco M., The GOODS Team, 2003a, in: The Mass of Galaxies at Low and High Redshift, ESO Astrophysics Symposia, p. 324, eds. Bender, R. & Renzini, A., Springer.

Dickinson M., Stern D., Giavalisco M., Ferguson H. C. et al., 2003b, to appear in ApJ Letters GOODS special issue (astro-ph/0309070)

Dunlop J., Peacock J., Spinrad H., Dey A., Jiménez R., Stern D., Windhorst R., 1996, Nature, 381, 581

Dunlop J.S., 2001, in van Bemmel I.M., Wilkes B., Barthel P., ed., FIRSED2000, New Astronomy Reviews, 45, Elsevier, p.609

Elston R., Rieke G.H., Rieke M.J., 1988, ApJ, 331, 77

Frayer D.T., Reddy N. A., Armus L., Blain A.W., Scoville N. Z., Smail I., 2003, AJ, in press (astro-ph/0310656)

Kauffmann G., Charlot S., 1998, MNRAS, 297, L23

Maihara T., Iwamuro F., Tanabe H., Taguchi T. et al., 2001, PASJ, 53, 25

Miyazaki M., Shimasaku K., Kodama T., Okamura S. et al., 2002, ApJ submitted (astro-ph/0210509)

Moustakas L. A., Somerville R. S., 2002, ApJ, 577, 1

Moustakas L., Casertano S., Conselice C., Dickinson M. E. et al., 2003, ApJL submitted (astro-ph/0309187)

Roche N. D., Dunlop J., Almaini O., 2003, MNRAS, 346, 803 (astro-ph/0303206)

Saracco P., Giallongo E., Cristiani S., D’Odorico S., Fontana A., Iovino A., Poli F., Vanzella E., 2001, A&A, 375, 1

Saracco P., Longhetti M., Severgnini P., Della Ceca R., Manucci F., Bender R., Dror N., Feulner G., Ghinassi F., Hopp U., Maraston C., 2003a, A&A, 398, 127

Saracco P., Longhetti M., Giallongo E., Arnouts S., Cristiani S., D’Odorico S., Fontana A., Nonino M., Vanzella E., 2003b, A&A submitted (astro-ph/0310131)

Smail I., Owen F. N., Morrison G. E., Keel W. C., Ivison R. J., Ledlow M. J., 2002, ApJ, 581, 844

Soifer B.T., Matthews K., Neugebauer G., Armus L., Cohen J.G., Persson S.E., Smail I., 1999, AJ, 118, 2065

Somerville R. S., Lee K., Ferguson H. C., Gardner Jonathan P., Moustakas L. A., Giavalisco M., 2003, to appear in ApJ Letters GOODS special issue (astro-ph/0309071)

Stanway E. R., Bunker A. J., McMahon R. G., 2003, MNRAS, 342, 439 (astro-ph/0302212)

Totani T., Yoshii Y., Iwamuro F., Maihara T., Motohara K., 2001, ApJ, 558, L87

Wehner E. H., Barger A. J., Kneib J.-P., 2002, ApJ, 577, L83

Willott C. J., Rawlings S., Jarvis M. J., Blundell K. M., 2003, MNRAS, 339, 173

Yan L., Thompson D., 2003, ApJ, 586, 765